Journal of Magnetic Resonance **138,** 232–243 (1999)
Article ID jmre.1999.1727, available online at http://www.idealibrary.com on IDEAL®

Pulsed Electron-Nuclear Double Resonance (ENDOR) at 140 GHz

M. Bennati,* C. T. Farrar,* J. A. Bryant,* S. J. Inati,* V. Weis,* G. J. Gerfen,†
P. Riggs-Gelasco,* J. Stubbe,* and R. G. Griffin*,[1]

*Francis Bitter Magnet Laboratory and Department of Chemistry, Massachusetts Institute of Technology, Cambridge, Massachusetts 02139; and †Department of Physiology and Biophysics, Albert Einstein College of Medicine, Bronx, New York 10461

Received September 25, 1998; revised February 3, 1999

We describe a spectrometer for pulsed ENDOR at 140 GHz, which is based on microwave IMPATT diode amplifiers and a probe consisting of a TE_{011} cavity with a high-quality resonance circuit for variable radiofrequency irradiation. For pulsed EPR we obtain an absolute sensitivity of 3×10^9 spins/Gauss at 20 K. The performance of the spectrometer is demonstrated with pulsed ENDOR spectra of a standard bis-diphenylene-phenyl-allyl (BDPA) doped into polystyrene and of the tyrosyl radical from *E. coli* ribonucleotide reductase (RNR). The EPR spectrum of the RNR tyrosyl radical displays substantial *g*-anisotropy at 5 T and is used to demonstrate orientation-selective Davies-ENDOR.

INTRODUCTION

Electron nuclear double resonance (ENDOR) spectroscopy, first proposed by Feher (*1*), is a well established technique for the determination of hyperfine interactions and spin density distributions in paramagnetic systems. With ENDOR, the NMR spectrum in the vicinity of a paramagnetic center can be indirectly detected through the electron spin, leading to much higher sensitivity than in conventional NMR experiments. ENDOR also offers substantially improved resolution compared to a typical EPR experiment and therefore represents a very powerful method for hyperfine spectroscopy. Developments in pulsed ENDOR techniques allow further possibilities for manipulating and extracting information from very complicated CW-ENDOR spectra. Reviews of Davies (*2*) and Mims (*3*) pulsed ENDOR and more advanced pulsed schemes are available (*4–6*).

In the past few years, improvements in high frequency microwave technology stimulated the development of EPR spectrometers operating in the millimeter regime (*7–14*). Although there are several attractive features of high field EPR spectroscopy, one of the most important is the improved orientation-selective excitation that can be achieved. Indeed, high field EPR spectra of systems with even small *g*-tensor anisotropy are typically dominated by the *g*-dispersion. Thus, microwave pulsed irradiation at arbitrary field positions in the EPR line excites only molecules with particular orientations of the *g*-tensor principal axis with respect to the magnetic field. This leads to a simplification of the data, where spectral information from only a few molecular orientations is observed. Further, high magnetic fields also lead to much higher resolution in ENDOR spectroscopy of low-gamma nuclei. For instance, in contrast to the situation at X-band, hyperfine spectra of ^{13}C, ^{15}N, ^{14}N, and ^{2}H are completely resolved from one another at our field of 5 T.

Therefore, the combination of high frequency EPR and ENDOR techniques is an attractive spectroscopic tool, as has been demonstrated at 95 GHz (*10, 15, 16*) and with CW experiments at 250 GHz (*17*). One challenging aspect of pulsed EPR/ENDOR at high frequencies is the design and implementation of efficient double resonance probes. The paucity of stable millimeter-wave power sources and amplifiers requires the use of high quality microwave cavities in order to obtain short microwave pulses ($t_{\pi/2} \ll 200$ ns). In contrast to standard 9 GHz EPR, high quality cavities ($Q \geq 3000$) can be employed at high frequencies without degrading the temporal resolution (i.e., dead time) of the pulsed spectrometer. The cylindrical TE_{011} cavity, introduced by Lebedev *et al.* (*18*) at 140 GHz, has been employed for pulsed EPR at millimeter wavelengths because of its high filling factor and ease of tuning. One disadvantage of this cavity is its miniature size, which requires small samples and external mounting of the radio frequency NMR coil for ENDOR, leading to compromises between RF penetration and the quality factor of the EPR cavity.

In this contribution we describe the design and operation of a new spectrometer for pulsed ENDOR at 140 GHz and demonstrate its capabilities with studies of the tyrosyl radical from *E. coli* ribonucleotide reductase (RNR). The microwave bridge described in detail by Prisner *et al.* (*11*) and further by Becerra *et al.* (*12*) was modified in order to achieve high-power microwave pulses. A double resonance probe for efficient EPR and NMR irradiation has been implemented together with a

[1] To whom correspondence should be addressed. E-mail: griffin@ccnmr.mit.edu.

1090-7807/99 $30.00

radiofrequency transmission line. Pulsed ENDOR performance at 140 GHz is demonstrated with a standard BDPA/polystyrene sample, where the ENDOR spectrum is rather simple because it is determined by only two sets of nonequivalent protons. Finally, the advantages of high-frequency orientation-selective ENDOR are demonstrated experimentally and with simulations of ENDOR spectra of the tyrosyl radical from *E. coli* RNR.

THE 140 GHz PULSED EPR/ENDOR SPECTROMETER

The pulsed EPR spectrometer consists of three main units: a magnet utilizing a ± 0.4 T superconducting sweep coil and a ^{2}H NMR field lock system, a 139.5 GHz microwave bridge with four phase capabilities operating in reflection mode, and a probe for EPR/NMR double resonance. These components are described in more detail in the following sections.

Magnet and Lock System

The polarizing magnetic field consists of a two-coil superconducting magnet (Magnex Corporation) with a 130-mm room-temperature bore. The larger main coil, operating in persistent mode, provides a static field of 5 T; the smaller superconducting sweep coil, located in the main coil bore, allows field sweeps of ± 0.4 T and access to systems with electron g-values in the range 1.84–2.16. The low current required for a ± 0.4-T field sweep (± 13 A) minimizes the helium boil-off rate.

For precise magnetic field measurements and field locking, an NMR teslameter that permits g-factor accuracies of $\leq 10^{-6}$ was implemented. The system, which is similar to that described by Un *et al.* (*19*), utilizes the dispersive component of the ^{2}H NMR signal from a ^2H_2O sample doped with $MnCl_2$ as an error signal in a feedback loop. The feedback signal controls the current amplifier that drives the sweep coil. When performing a field step, the RF excitation frequency of the deuterium NMR probe is swept under computer control, causing a change in the sweep coil current. Thus, the magnetic field step is determined by the width of the deuterium NMR line, which is $\sim$100 Hz (0.015 mT for deuterium). The field resolution is not limited by the current stability of the sweep coil power supply (KEPCO), specified to 0.01% of the current value, since the large inductance of the sweep coil ($L = 24.0$ H) and small resistance of the sweep coil lead ($R = 0.5\ \Omega$) act to filter out any high-frequency power supply voltage fluctuations due to the very long time constant ($\tau = L/R \sim 48$ s) for the current response. For instance, for $g = 2$ resonances a sweep coil current of about 1 A leads to a specified current stability of 0.1 mA, corresponding to a predicted field instability of 3.1 μT, which is greater than that observed experimentally. Field stability and resolution were tested experimentally with the narrow EPR line of perylene-PF_6, an organic conductor radical cation salt. At 140 GHz the single-crystal ($0.1 \times 0.15 \times 0.1$ mm) EPR spectrum reveals a two-component EPR line with a total width of 0.05 mT. CW-EPR spectra were recorded with a minimum field step of 1 μT, representing a field resolution of 0.2 ppm of the central field. Consistently, the pulsed EPR signal of perylene in the time domain (FID) displays a frequency noise of about 30 kHz between consecutive shots, yielding a field stability of $\sim$0.2 ppm in agreement with the CW experiment.

Microwave Bridge

The microwave bridge described previously (*11, 12*) has been significantly modified in order to achieve higher microwave pulse power and four-phase switching capability. Since we use a heterodyne detection scheme, the main microwave sources consist of two InP Gunn diodes (Millimeter-Wave Oscillator) operating at 139.5 (main source) and 139.95 GHz (reference) locked to a 50 MHz source (FM noise of -150 dBc/Hz at 1 kHz offset). The difference between the main and reference frequencies represents our intermediate frequency of 450 MHz. Microwave power amplification is achieved with an IMPATT diode network (Donetsk Physico Technical Institute). A combination of fast amplitude and 0°–90°, 0°–180° phase switches with three IMPATT diode oscillators leads to 37 mW output power and microwave pulses with $\leq$10 ns rise and fall times. However, the FM noise of IMPATT diodes exceeds that of frequency locked Gunn diodes, because of the intrinsically different methods of generating microwaves (avalanche emission versus oscillation of thermally excited electrons). In order to minimize any increase in the noise figure of the spectrometer, the 139.5 GHz IMPATT oscillator network is injection locked by our 139.5 GHz Gunn diode, which was measured to be free ($<$50 dB) of adjacent harmonics of the primary 50 MHz source. The reference arm, which drives the high-frequency mixers, is unaffected by the IMPATT amplifier. Finally, the microwaves are conducted to the resonator using a combination of oversized and fundamental waveguides (WR-42 and WR-8), tapers, and bends. Insertion losses in the circulator and propagation pathway (8–9 dB) attenuate the incident power at the resonator to approximately 5 mW.

ENDOR Probe

Our current resonator is a TE_{011} cylindrical cavity suitably modified to permit RF irradiation during the ENDOR experiment. The cavity radius r and length d are chosen so that $2r/d = 1$, the condition for optimal Q in the TE_{011} mode (*20*). Tuning is achieved with a fixed and a moveable plunger, while microwave coupling into the cavity is established through a circular, centered iris and can be adjusted by rotating the wave guide with respect to the axis of the resonator. The performance of the resonator depends critically on the iris thickness, diameter, and length of the fixed plunger. Generally, the length of the fixed plunger is optimized for each sample depending on

its dielectric loss. However, the samples used most frequently, such as frozen solutions and powders, display low dielectric constants and are investigated in 0.5 mm OD capillaries combined with a single plunger of fixed length. In contrast, aqueous solutions require shorter plungers and thinner capillary tubes (0.17 mm OD). An empirically optimized iris diameter of 0.66 mm and thickness of 0.12 mm were found for WR-8 wave guide of 1 × 2 mm cross section.

For the ENDOR probe we first followed the design described by other authors (*10, 15*), where the NMR coil is mounted external to the cavity and RF field penetration into the resonator must be optimized. Since the skin effect prevents RF penetration into a solid metal cavity, it is necessary to cut slots in the resonator walls finding a compromise between RF penetration and microwave losses. RF penetration can be further increased if the formation of RF induced eddy currents in the resonator walls and plungers are suppressed by cutting slots through the entire length of the metal cylinder, a concept tested and discussed previously for a 95 GHz resonator (*21*). For our 140 GHz resonator we employ 3 slots 0.5 mm in width and 0.38 mm apart along the active cavity volume and further slots 0.25 mm in width through the entire length of the metal cylinder. The additional slots are narrower in order to maintain mechanical stability of the soft silver cylinder. The resonator wall thickness amounts to 1.13 mm. Plungers are fabricated from insulating Kel-F with copper plated end faces. The resonator assembly is shown in Fig. 1. A new improved design of the cylindrical TE_{011} cavity, which permits optimal RF penetration without power losses, has been implemented recently and will be presented in a separate paper.

In ENDOR experiments it is necessary to sweep the RF over a large frequency range (typically several megahertz) while concurrently maintaining a high quality factor in the RF circuit. Initially, broadband RLC resonant circuits were tested in combination with our TE_{011} resonator but were of low RF efficiency, particularly at high frequencies in the region of the ^{1}H resonance ($^{H}\nu_0 = 212$ MHz at our $g = 2$ resonance field). We therefore adopted the circuit shown in Fig. 2a, which is typical in solid-state NMR and consists of a high-quality LC parallel circuit with variable matching and tuning capacitors. High-voltage variable capacitors are mounted on top of the probe, outside of the cryostat, to prevent arcing and temperature-dependent capacitance changes when cooling with helium gas. A semirigid cable of approximately $n\lambda/2$, where n is an integer and λ is the RF wavelength, connects the capacitors to the NMR coil, which is a split solenoid with 2–4 turns mounted perpendicular to the resonator axis. To maintain tuning and matching during the RF sweep, we utilize a computer-controlled high-precision micrometer and a digital encoder (Oriel Corporation) that drives the tuning and matching capacitors. For a high-Q circuit, the ratio of the capacitors at resonance is given by a constant (*22*),

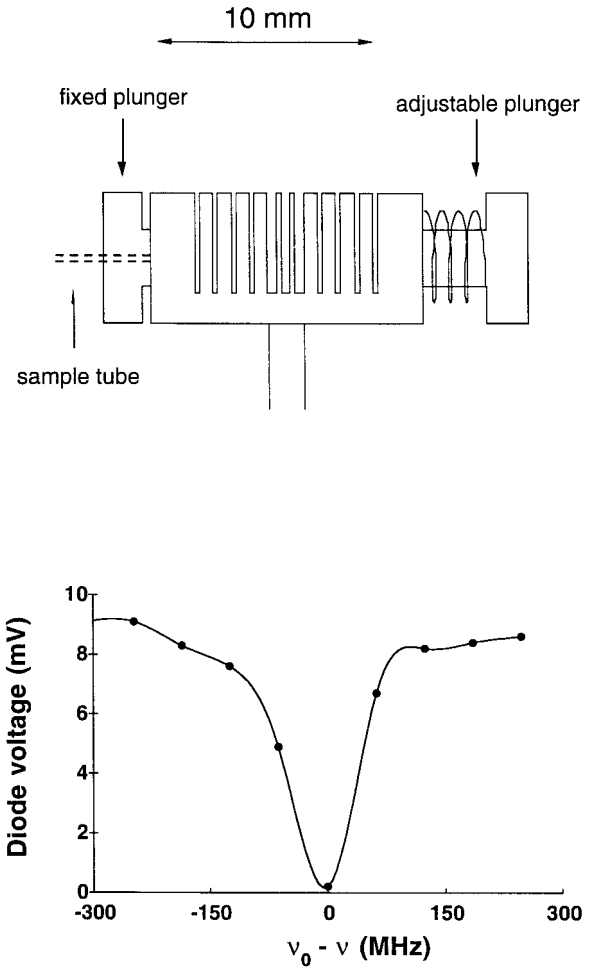

FIG. 1. *Top:* Side view of the 140 GHz cylindrical resonator used for ENDOR displaying the different slots for improved RF penetration, the fixed and movable plungers, and the sample tube. *Bottom:* Tuning curve of the ENDOR resonator loaded with a 0.4 mm (ID) capillary and solid BDPA/polystyrene sample.

$$\frac{C_2}{C_1} = \sqrt{\frac{r}{R_T}}, \qquad [1]$$

where r is the resistance of the coil and R_T is the impedance of the transmission line. Therefore, a single micrometer can control both capacitors simultaneously through a gear system with the appropriate gear ratio. With this arrangement we typically cover a sweep range of about 20 MHz around the ^{1}H free Larmor frequency. A calibration curve allows the setting of the micrometer position for tuning and matching during a frequency scan and typical RF steps of 50 kHz are achieved in ~3 s. For low gamma nuclei, such as ^{13}C, ^{15}N, ^{14}N, and ^{2}H, broadband circuits with characteristics of low-pass filters also permit highly efficient RF irradiation, as described by Höfer (*23*) and Disselhorst *et al.* (*15*) and are preferentially used because of the ease of construction.

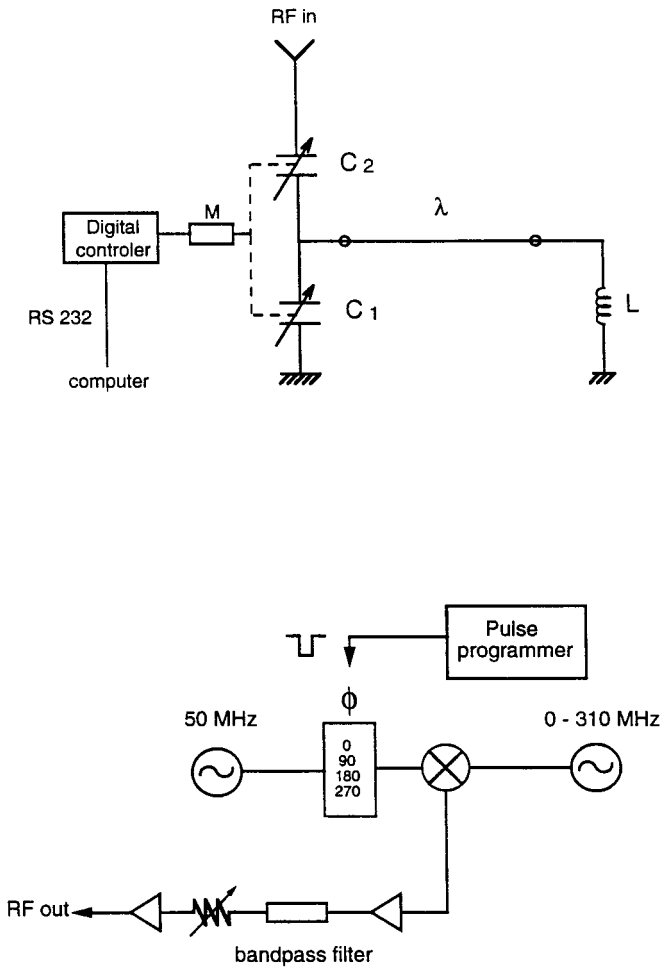

FIG. 2. (a) Schematic representation of the NMR circuit for the ENDOR probe. C_1 and C_2 are variable capacitors controlled by a high-precision micrometer (M). The micrometer position is set by the computer through a digital controller. (b) Diagram of the NMR transmission line for variable frequency ranges and four-phase capability.

The frequency variation in the RF is generated with a PTS synthesizer. Pulses and four orthogonal phases are formed at an intermediate frequency of 50 MHz and are controlled by a pulse programmer (Interface Technology). RF amplification is performed over 10–300 MHz with an American Microwave Technology amplifier ($P_{max} \sim 500$ W in pulsed operation). The transmission line is represented schematically in Fig. 2b.

SPECTROMETER PERFORMANCE

ENDOR Probe

The performance of the ENDOR probe was assessed in different ways. Initially, quality factors of the cylindrical cavity were measured using a microwave frequency sweeper (Insight Products Corp.) with a calibrated frequency output (20–180 GHz) and steps of 62 MHz. The reflected power was monitored with a crystal detector. A typical measurement is displayed in Fig. 1 (bottom) for the loaded ENDOR cavity, containing a BDPA/polystyrene powder sample loaded in a 0.5 mm (OD) quartz tube. We find a $Q > 2200$ and 1400 for unloaded and loaded cavities, respectively. Quality factors larger than ~2200 could not be measured because of the limited step size of the sweeper.

In addition, the 90° microwave pulse length ($t_{\pi/2}$) was estimated in two pulse spin-echo experiments. We used dilute samples of a symmetric trityl radical (NYCOMED Innovation AB), which displays very long relaxation times at low temperature ($T_{1e} \sim 1$ s at $T = 15$ K; the spin-echo intensity is constant for pulse spacings ≤ 800 ns). The 90° pulse length was obtained by varying the incident microwave power for fixed pulse lengths as well as by varying the pulse lengths for a fixed maximum power. Accordingly, the cylindrical resonator without slots yielded 90° pulses of ~60 and 70 ns at low and room temperature, respectively. With the ENDOR resonator we obtained values in the range 90–110 ns.

A knowledge of the loaded Q and incident power into the resonator (5 mW, see above), and assuming a typical conversion factor c for cylindrical cavities of 30 $\mu T/\sqrt{W}$ (experimental values are between 20 and 50 $\mu T/\sqrt{W}$ (*24*)), permits an estimate of the theoretical field strength B_1 for the ENDOR cavity using

$$B_1 = c\sqrt{Q \cdot P}. \qquad [2]$$

We arrive at $B_1 = 0.08$ mT, in agreement with the experimental 90° pulse length of 100 ns.

The efficiency of the RF irradiation was first tested by measuring the Rabi oscillation of the nuclear sublevels in an ENDOR experiment. As a standard sample we use the solid organic radical bis-diphenylene-phenyl-allyl (BDPA) doped in polystyrene (1%) at room temperature. The Rabi oscillation is usually monitored on the maximum of the ENDOR line at 209 MHz using a Mims-ENDOR type of EPR preparation–detection scheme and recording the electron spin echo intensity as a function of the RF pulse length. A typical curve is displayed in Fig. 3 for an ENDOR probe with a four-turn RF coil and an RF power of 450 W. The RF field strength B_2 can be estimated considering the expression for the nutation of a spin-$\frac{1}{2}$ nucleus under the effect of a magnetic field $B_2 = \omega/\gamma$ perpendicular to the external field B_0 (*23*):

$$\langle I_z \rangle = \frac{\Delta\omega^2 + \omega^2 \cdot \cos(\omega_{eff} t_{RF}) \cdot \exp(-t_{RF}/T_r)}{\omega_{eff}^2}, \qquad [3]$$

where $\omega_{eff} = \sqrt{\Delta\omega^2 + \omega^2}$. Here $\Delta\omega$ is the resonance offset with respect to the irradiation frequency and t_{RF} is the RF pulse length. RF-field inhomogeneities and spectral diffusion lead to

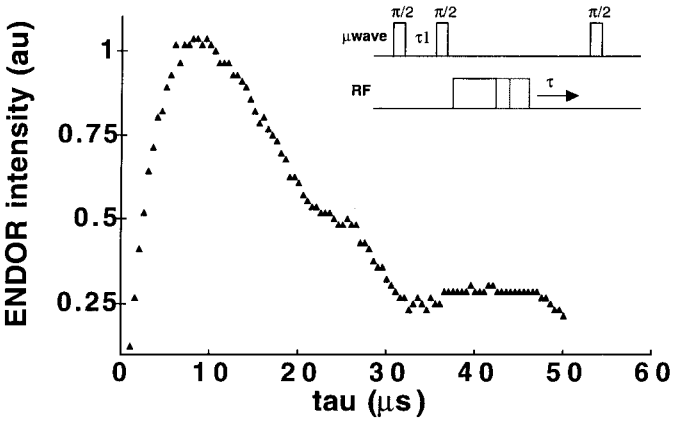

FIG. 3. Rabi oscillation of the protons in BDPA for RF excitation at ν = 209 MHz, T = 293 K. Mims ENDOR, MW $\pi/2$ pulse: 110 ns, pulse interval $\tau 1$ = 200 ns, RF power 450 W.

a damped oscillation and are included in the time constant T_r. In our case the pulse excitation width is much smaller than the ENDOR line; therefore, all $\langle I_z \rangle_i$ contributions at a frequency offset $\Delta\omega_i$ covered by the excitation width have to be integrated to obtain a total $\langle I_z \rangle$. Different nutation frequencies of single $\langle I_z \rangle_i$ lead to a higher observed nutation frequency compared to the line at $\Delta\omega = 0$. The experimental curve displayed in Fig. 3 shows a more complicated behavior than represented by integrating Eq. [3] over the frequency offset $\Delta\omega_i$, likely due to fast electron and nuclear relaxation effects at room temperature. However, the position of the first maximum is well resolved at 8.6 μs. Taking into account the effect of off-resonance contributions, this value should lead to a 180° pulse length on the order of 10–15 μs. In order to determine the 180° pulse length more precisely, we used the ENDOR probe together with a 200 MHz solid-state NMR magnet and spectrometer (*12*). A liquid H_2O sample was inserted into the resonator and the 180° pulse length of the protons was observed directly. The on-resonance, narrow proton line could be inverted using a 24 μs 180° pulse with 140 W RF power delivered to the probe. This corresponds to about 13 μs 180° pulses with the 450 W power available in the ENDOR experiment, in good agreement with the estimate from the ENDOR Rabi oscillation.

For standard Davies- and Mims-ENDOR experiments, which suffer from power broadening, pulse lengths of this magnitude are a good compromise between sensitivity requirements and linewidth resolution. For coherence transfer ENDOR experiments, much shorter pulse lengths and correspondingly larger excitation bandwidths are desirable, which will require improvement of the resonator design.

EPR Sensitivity

One advantage of performing double resonance experiments at high microwave frequencies is the high absolute sensitivity achieved in the EPR experiment, which is reflected in the ENDOR spectrum. This is particularly pertinent when small amounts of sample are available, as is often the case with biological compounds. Therefore, we provide a brief discussion of the sensitivity of our spectrometer. A detailed sensitivity analysis of the previous 140 GHz spectrometer was reported by Prisner *et al.* (*11*). We measured the sensitivity of the CW experiment using standard water/glycerol solutions of the trityl radical at room temperature contained in 0.1 mm ID quartz tubes in order to minimize dielectric losses. The experimental sensitivity, E [spins/Gauss], can be obtained from the formula (*20*)

$$E = \frac{N}{(S/N) \cdot n \cdot \Delta H_{pp}^2}, \qquad [4]$$

where N is the total number of spins, S/N is the peak-to-peak signal-to-noise, n is the number of lines, and ΔH_{pp} is the peak-to-peak width of the derivative EPR spectrum. We arrive at $E = 1.4 \times 10^8$ spins/Gauss, a result that compares favorably with previous experimental values of 10^9 spins/Gauss (*11*, *12*). The improvement in sensitivity is primarily due to improved cavity construction and to the incorporation of a new low-noise 50 MHz source to which the microwave sources are locked.

The sensitivity of the pulsed EPR spectrometer was determined in a two-pulse spin-echo experiment, using a trityl radical solution with an inhomogeneous linewidth of ~1.5 mT. We follow the definition for E proposed by Prisner (*25*),

$$E = \frac{N}{(S/N)(2m_I + 1)\Delta H_{1/2}} e^{-2\tau/T_2}, \qquad [5]$$

where S/N is the signal-to-noise (in a single shot) of the peak-echo amplitude compared to the rms noise with a detection bandwidth matched to the echo shape. We arrive at $E = 3 \times 10^9$ spins/Gauss at T = 20 K. This sensitivity limit permits pulse EPR/ENDOR studies of samples in the 10^{-3}–10^{-4} M concentration range, which is typical for biological proteins and opens a wide range of applications for pulsed EPR techniques in the 2 mm regime.

As expected, the absolute sensitivity of the pulsed mode is lower than CW mode operation because of the narrower detection bandwidth of the latter experiment. Nevertheless, the measured sensitivities cannot be compared directly because of the different time constants associated with the two experimental modes. Moreover, we found that the CW experiment is sensitive to baseline distortions due to microphonics arising from the B_0 modulation coils. The modulation coils are located in the cryostat inserted in the narrow bore of the superconducting magnet and are difficult to mechanically decouple from the probe. This can lead to a large baseline offset at the lock-in detection frequency.

ENDOR Performance

Two standard pulsed ENDOR experiments, Davies- and Mims-ENDOR, have been employed in order to demonstrate the performance of the spectrometer. As typical experimental parameters we use $\pi/2$ microwave pulses of 100 ns and RF π pulses of 10 μs. Baseline correction is performed by subtracting two consecutive sequences and toggling the RF pulse. Spectra from 1% BDPA in polystyrene at room temperature were obtained from a single scan of the RF frequency with an integration averaging of 100 shots/point.

BDPA is a stable radical with an alternating spin density localized on the diphenylene rings (Fig. 4, top). Two hyperfine couplings result from two sets of eight magnetically equivalent ring protons, yielding a pair of doublets in the ENDOR spectrum. The EPR line is nearly Gaussian with a width of ~1 mT, which is determined by the hyperfine splitting of the 16 protons and a small g-anisotropy visible upon deuteration. Although the ENDOR lines are broad because of hyperfine anisotropy and power broadening, two splittings are easily distinguished, and therefore the spectra are useful for comparing lineshape

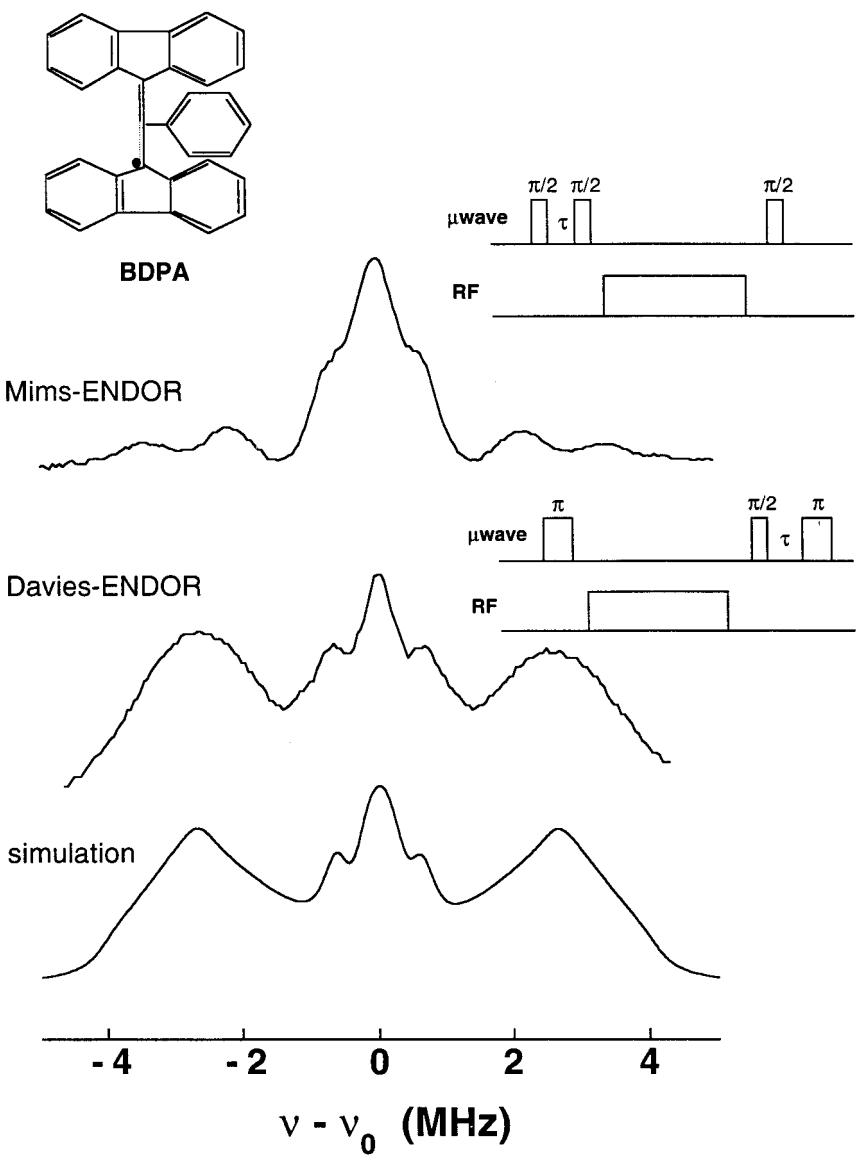

FIG. 4. ^{1}H ENDOR spectra of BDPA in polystyrene (1%) at room temperature, ν_0 = 211.7 MHz. Mims-ENDOR (top), Davies-ENDOR (middle), Davies-ENDOR simulation (bottom). Experimental parameters: MW π pulse: 200 ns, τ (Mims) = 200 ns, τ (Davies) = 400 ns, RF π pulse: 10 μs, RF power: 400 W, 100 averages/point, single scan spectra. Simulation parameters used are: g_x = 2.00263, g_y = 2.00260, g_z = 2.00257. The following hyperfine constants are in megahertz and represent the absolute values: ^1A_x = 1.0, ^1A_y = 1.0, ^1A_z = 1.26, ^2A_x = 7.7, ^2A_y = 5.3, ^2A_z = 2.0. *Inset:* Structure of BDPA radical.

effects arising from preparation and detection pulses. Room-temperature spectra are displayed in Fig. 4.

Mims-ENDOR, which is a stimulated echo sequence with a RF pulse at a nuclear transition inserted between the second and third mw-pulses ($\pi/2$–τ–$\pi/2$–RF–$\pi/2$), is known to preferentially detect small hyperfine couplings. This is demonstrated by the experimental comparison of Mims- with Davies-ENDOR spectra in Figs. 4a and 4b. Additionally, a strong ^{1}H matrix peak is observed at the Larmor frequency. However, the Mims-ENDOR intensity suffers from a periodic dependence on the pulse spacing τ, given by $I_{(\mathrm{ENDOR})} \sim 1 - \cos(2\pi A\tau)$, where A is the hyperfine constant and τ is the time between the two $\pi/2$ excitation pulses. The spectrum represented in Fig. 4a was recorded with $\tau = 200$ ns, which leads to clearly visible intensity minima at $\Delta\nu \cong \pm 2.5$ MHz. Davies-ENDOR (π–RF–$\pi/2$–τ–π) (*2*) is the more attractive technique because of limited lineshape distortion, essential for accurate simulations. Spectra are affected by an intensity "hole" centered at $\Delta\nu = 0$, which reflects the excitation band width of the preparation pulse. Note that the doublet at ± 0.7 MHz is much weaker than the second one at ± 2.5 MHz, although they are determined by the same number of protons. We find that the intensity of the center increases for longer and weaker preparation pulses, but the sensitivity also degrades. The overall signal-to-noise is comparable to that of Mims-ENDOR, and therefore Davies-ENDOR was typically used. A more detailed discussion of the lineshape is given in the next section.

SIMULATION OF DAVIES ENDOR SPECTRA

For calculating Davies ENDOR spectra, we utilize analytic expressions for the ENDOR lineshapes as a function of the preparation and detection pulse as outlined by Grupp and Mehring (*4*). The computation involves simulation of the EPR spectrum in order to obtain the *g*-values and an initial set of hyperfine couplings. During computation of the EPR spectrum the orientations that match the pulse excitation profile at a given external field are extracted and the corresponding ENDOR frequencies are computed. The resulting ENDOR spectrum is a sum of the orientation-selected hyperfine spectra convoluted with preparation and detection functions. EPR and ENDOR frequencies are obtained by diagonalizing the Hamiltonian for interacting electron and nuclear spins and are given by the expressions

$$\nu_{\mathrm{S}} = \frac{g\beta_{\mathrm{e}}B_0}{h} - \sum_{i=1}^{n} m_{\mathrm{I}}^{i}(A^{i}(+) - A^{i}(-)) \quad \text{for EPR} \qquad [6]$$

$$\nu_{\mathrm{I}}^{i}(\pm) = A^{i}(\pm) \quad \text{for ENDOR} \qquad [7]$$

$$A(\pm) = \pm 0.5A_{zz} - \nu_{\mathrm{oI}}, \qquad [8]$$

where g and A are the angular-dependent g-factor and hyperfine constant, respectively, the summation runs over the i nuclear spins, and the symbol $\pm$ refers to the sign of electron spin manifold m_s. The angular dependence of A is numerically computed with two consecutive Euler rotations, first into the g-tensor principal axis frame ($R_{\alpha,\beta,\gamma}$), then into the laboratory frame ($R_{\theta,\varphi}$).

Effects produced by the preparation and detection pulses in Davies-ENDOR can be derived from Eq. [3]. The complete ENDOR response is written as

$$I_{\mathrm{ENDOR}}(\Delta\omega_{\mathrm{I}}) = I_{\mathrm{N}}(\Delta\omega_{\mathrm{I}}) \int_{-\infty}^{+\infty} d\Delta\omega_{\mathrm{S}} g(\Delta\omega_{\mathrm{S}}) \times f_{\mathrm{p}}(\Delta\omega_{\mathrm{S}}, \Delta\omega_{\mathrm{I}}) f_{\mathrm{d}}(\Delta\omega_{\mathrm{S}}), \qquad [9]$$

where the integral runs over all EPR offset frequencies $\Delta\omega_{\mathrm{S}}$, I_{N} is the normalized hyperfine spectrum given by the foregoing transition frequencies, f_{p} and f_{d} are preparation and detection functions as reported in (*4*), and $g(\Delta\omega_{\mathrm{S}})$ is the EPR lineshape function. In the continuum approximation used here, the excitation bandwidth is assumed to be much smaller than the EPR linewidth, and $g(\Delta\omega_{\mathrm{S}})$ can therefore be neglected because it is nearly constant over the excitation profile. For a 180° preparation pulse and a spin echo detection sequence, the previous equation can be approximated by (*23*)

$$I_{\mathrm{ENDOR}} = \frac{\omega^{*2}_{1\mathrm{s}}}{\Delta\omega_{\mathrm{I}}^{2} + \omega^{*2}_{1\mathrm{s}}}, \qquad [10]$$

with $\omega^{*}_{1\mathrm{s}} \approx 0.7\ \omega_{1\mathrm{s}}$, where the phenomenological scaling factor of 0.7 includes relaxation by spin diffusion effects. Finally, RF power broadening leads to ENDOR linewidths on the order of $1/t_{\mathrm{RF}}$, where t_{RF} is the RF pulse length. This can be derived directly from Eq. [3]. For a 10 μs pulse the ENDOR linewidth is therefore $\sim$0.1 MHz. For faster computation, the ENDOR lineshape is approximated by a Lorentzian line and the lineshape convolution is performed in the time domain.

An example of the calculated Davies-ENDOR spectrum of BDPA for a 200 ns 180° preparation pulse is displayed in Fig. 4 together with the experimental spectrum. The calculation is performed for 16 nuclear spins coupled to the electron spin. Although there are only two inequivalent sets of protons, the full spin space must be considered for computation of the EPR line and for proper orientation selection. The weak intensity of the doublet at ± 0.7 MHz compared to the doublet at ± 2.5 MHz is a direct consequence of the preparation pulse. The matrix peak is simulated by a simple Gaussian line and is weighted in order to obtain the observed intensity. The experimental spectrum was recorded in the center of the EPR line, which results in excitation of a wide range of molecular orientations. This is reflected in the broad, almost featureless powder pattern for the larger hyperfine coupling. The calcu-

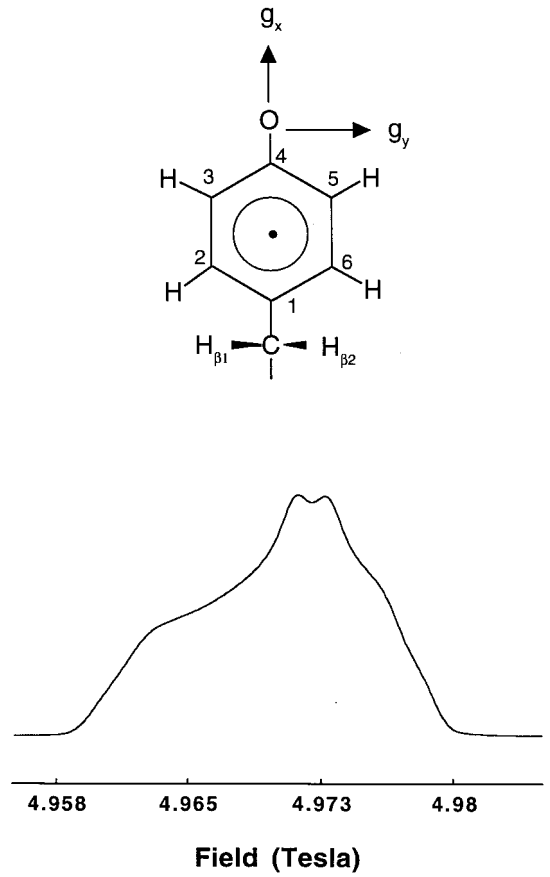

FIG. 5. *Top:* Chemical structure of the tyrosyl radical. The directions of the g-tensor principal axes and the labeling of the protons are shown as discussed in the text. *Bottom:* 140 GHz stimulated echo-detected EPR spectrum of 1 mM tyrosyl radical from *E. coli* RNR, $T = 15$ K. Experimental parameters: MW $\pi/2$-pulse: 110 ns, pulse interval $\tau = 300$ ns, 300 averages/point, single scan spectrum.

lated spectrum shows slightly sharper features, a difference that could arise from power broadening effects and finite angular resolution in the powder pattern. Neither the experimental or simulated ENDOR spectra change considerably at other EPR excitation fields, consistent with a very small g-anisotropy.

ORIENTATION-SELECTIVE ENDOR OF THE TYROSYL RADICAL FROM *E. coli*

A major application of high-field ENDOR consists of performing hyperfine measurements at different field positions in the EPR line corresponding to excitation of highly selected molecular orientations. The g-anisotropy dispersion scales with the external magnetic field, and therefore the 140 GHz ENDOR spectra reveal field-dependent powder patterns that provide a large number of constraints for the determination of the hyperfine couplings. We demonstrate the advantages of 140 GHz orientation-selective ENDOR with spectra of the tyrosyl radical from *E. coli* RNR.

Figure 5 shows a schematic representation of the tyrosyl radical together with the 140 GHz echo-detected EPR spectrum obtained at 10 K. The sample consists of 0.25 μl of an aqueous protein solution containing 1 mM tyrosyl radical. Note the excellent signal-to-noise obtained in a single-scan spin-echo experiment (experimental parameters are given in the figure caption), which allows the performance of pulsed ENDOR even on the low-intensity edges ($B_0 = 4.96$ and 4.979 T) of the EPR line shape. The shape of the EPR spectrum is mainly determined by g-anisotropy, with values of $g_x = 2.00912$, $g_y = 2.00457$, and $g_z = 2.00225$ (*26*). The orientation of the g-tensor principal axis system was proposed by Gerfen *et al.* (*26*), with the principal axis belonging to g_x lying parallel to the C_4–O bond, and g_z being normal to the ring plane (see Fig. 5). Six protons are coupled to the unpaired electron spin, two magnetically inequivalent β-methylene protons and two sets of equivalent ring protons (2,6 and 3,5), resulting in four different hyperfine couplings. Figure 5 displays the labeling of the protons as described in the text. ENDOR studies at 9 GHz (*27*, *28*) revealed that the β_1-methylene proton and the 3,5-ring protons are strongly coupled to the electron spin, resulting in very large isotropic hyperfine splittings ($A_{iso} > 18$ MHz), which are directly observable in the EPR spectra. In contrast, analysis of the weakly coupled protons is much more complex, since these are detectable only in ENDOR spectra and the resonances strongly overlap the matrix peak. However, at 140 GHz the congested small coupling region can be resolved with

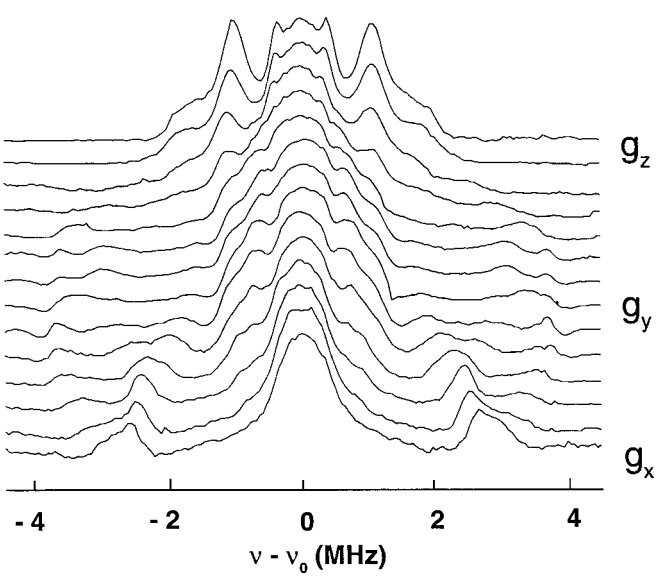

FIG. 6. Orientation-selective Davies ^{1}H-ENDOR of the tyrosyl radical of RNR from *E. coli*. Spectra are displayed starting from the low-field edge (g_x) to the high-field edge (g_z). Experimental parameters: $T = 15$ K, MW π pulse: 240 ns, RF π pulse: 10 μs, RF power: 400 W, 100 averages/point, single scan spectra.

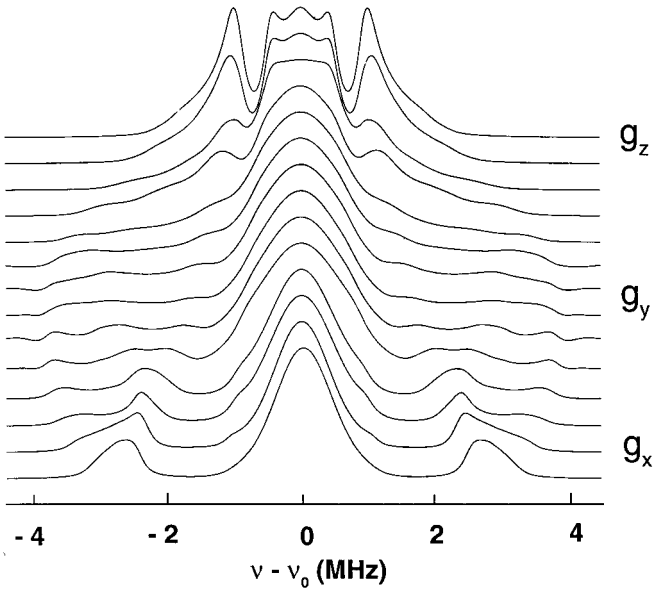

FIG. 7. Simulated ENDOR spectra of the tyrosyl radical from the low-field edge (g_x) to the high-field edge (g_z). Simulation parameters for the hyperfine couplings are given in Table 1.

orientation-selective measurements and unambiguous assignment of the hyperfine couplings is performed.

Davies ENDOR spectra were recorded at ~15 K for different excitation positions in the EPR line, with approximately 2 mT steps from g_x to g_y (low-field edge to center of the spectrum) and 1 mT steps from g_y to g_z (center to high-field edge). In Fig. 6 we show the magnetic field dependence of the ENDOR spectra in the small coupling region, i.e., for $A < |5|$ MHz. The shape of the powder pattern changes dramatically with the magnetic field, suggesting strongly anisotropic hyperfine couplings. A very intense matrix peak is also observed in the center, which is due to pure dipolar interactions with the protein surroundings. Experiments with a D_2O exchanged matrix lead to analogous spectra with slightly narrower lines, indicating that all relevant features are related to the 2,6-ring and β_2-methylene tyrosyl protons and no additional hydrogen bonded protons are involved. This is consistent with recently reported ^{2}H-ENDOR Q-band data of van Dam *et al.* (*29*).

When hyperfine spectra of different protons overlap, rough assignment of hyperfine couplings can be done if the hyperfine tensor principal axes are approximately collinear with the g-tensor axes. At magnetic fields close to g_z and g_x this leads to "single-crystal-like" spectra; however, at intermediate fields the powder pattern can still be complicated. We expect this to be the case for both 2,6- and β_2-methylene protons of the tyrosyl radical, where the y-axis of the hyperfine tensor points along the C–H bond and the z-axis is approximately normal to the ring plane. Sharp features are recorded at magnetic fields close to g_z. The 2,6-proton peaks should appear twice as intense as those from the β_2-methylene, and therefore the

TABLE 1
Principal Hyperfine Values and Orientations[a] Used in Simulations of the ENDOR Spectra

Protons	A_x (MHz)	A_y (MHz)	A_z (MHz)	ϕ (deg)	ψ (deg)	Ref.
2 or 6	+5.0	+7.6	+2.1	44		*28*
2 or 6	+4.9	+7.7	+1.9	25	|10|	This work
β_2	+2.1	−5.0	−4.0	−26		*28*
β_2	−2.1	6.2	−1.0	−30	−8	This work
3 or 5	−26.4	−8.1	−19.3			This work[b] and *26*
β_1	58.0	55.4	52.4			This work[b] and *26*

[a] The angle ϕ describes a rotation in the xy-plane of the proton bond direction toward the direction of the g_y tensor principal axis. The angle ψ describes a rotation in the yz-plane of the proton bond direction toward the ring plane normal, i.e., the direction of the g_z-tensor principal axis.

[b] Hyperfine values obtained from simulation of the 140 GHz echo detected spectrum, in agreement with ref. (*26*).

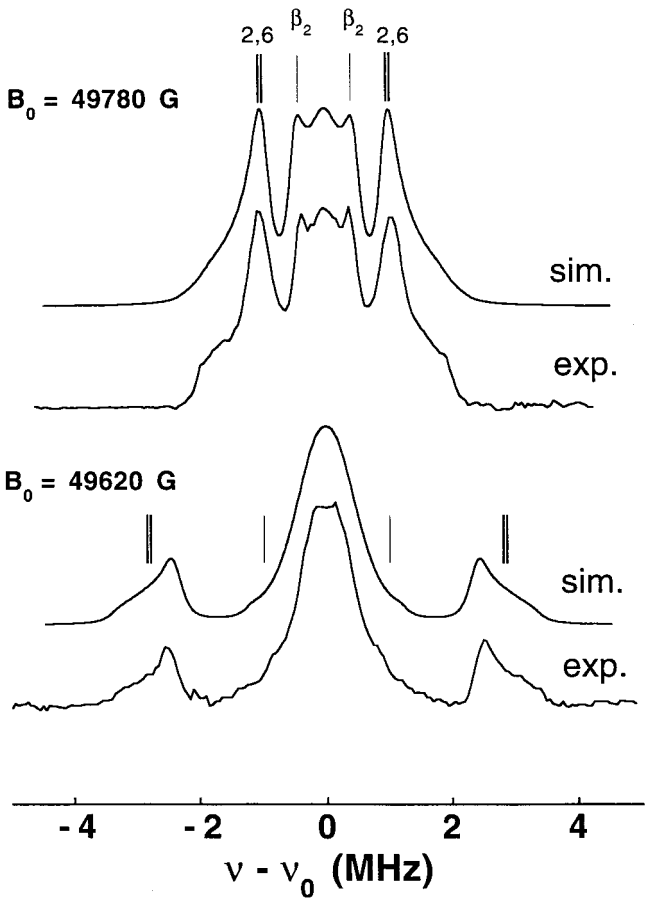

FIG. 8. Comparison of experimental and simulated ENDOR spectra of the tyrosyl radical at the low-field edge (g_x) and at the high field edge (g_z). The assignment of peaks to the β_2-methylene and to the 2,6 ring protons is indicated.

strong doublet at ±1.0 MHz arises from the 2,6 protons as suggested previously (*28*). In addition, our spectra show well-resolved shoulders and a narrow doublet at ±0.5 MHz. A correct analysis of these features requires simulations of the ENDOR lineshape. At magnetic fields close to the g_x-edge we observe strong peaks at around ±3 MHz arising from the 2,6-protons. The line shape of the peaks deviates from a "single-crystal-like" pattern. In fact, the *y*-axis of the 2,6-proton hyperfine tensor is rotated by about 30° in the *xy*-plane and mixing of the A_x and A_y tensor components is expected. We anticipate that the ENDOR spectra in the field range between g_x and g_y are primarily determined by the 2,6 protons because the couplings of the β_2-methylene protons are much smaller and overlap with the matrix peak. Therefore, the high spectral resolution in this field region allows the angular dependence of only one hyperfine tensor to be followed with accuracy.

Figure 7 shows the field dependence of the calculated ENDOR spectra of the RNR tyrosyl radical at different field positions in the EPR line. The calculation is performed with all six protons, but only the small coupling region is displayed. For a better representation, the matrix peak was simulated by a simple Gaussian line, and its width and intensity were varied at different field positions. As a starting parameter set we used the hyperfine tensor values reported by Hoganson *et al.* at 9 GHz (*28*), which are listed for reference in Table 1. The hyperfine parameters were iteratively varied in order to fit our experimental data. The values proposed by Hoganson *et al.* provide an excellent fit of our data in the magnetic field region between g_x and g_y. However, discrepancies were found for the region between g_y and g_z, which necessitated reassignment of the hyperfine couplings of the β_2-methylene proton. Our optimized parameter set is assembled in Table 1.

First, we note that a salient feature of the experimental spectra is the presence of two doublets and shoulders at magnetic fields close to g_z. Previous studies with 9 GHz ENDOR (*27, 28*) were not able to satisfactorily resolve the doublet at ±0.5 MHz, and therefore the shoulders at ±2.1 MHz were assigned to the A_z couplings of the β_2-methylene proton. However, our simulations indicate that this assignment is not compatible with our experimental spectra and their magnetic field dependence. Instead, we assign the narrow doublet at ±0.5 MHz to the β_2-methylene proton, and we show that the shoulders at ±2.1 MHz arise from the 2,6 protons, if mixing of A_z and A_y tensor components is assumed due to small torsional angles of the C–H bond out of the ring plane (~10°). An experimental spectrum and simulation plotted together in Fig. 8 (top) are indicative of the sensitivity of the 140 GHz ENDOR

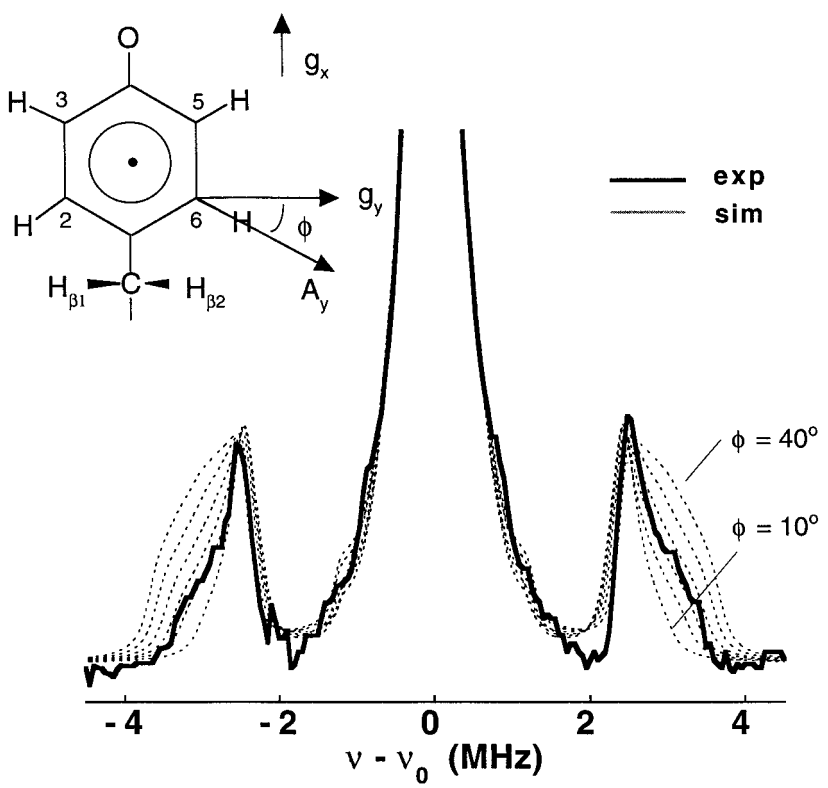

FIG. 9. Simulated ENDOR spectra of the tyrosyl radical at the low magnetic field edge (g_x) for different angles ϕ of the 2,6-proton bond (which defines the direction of the A_y principal axis) to the direction of the g_y principal axis. Simulation curves (dotted lines) are displayed for ϕ = 10°, 20°, 25°, 30°, 35°, 40°. The angle ϕ is related to the Euler angle α by $\alpha = 90 - \phi$.

spectra to such small angle variations. Simulations also reveal that the A_y hyperfine coupling of the β_2-methylene proton is larger than previously reported. Specifically, the A_y coupling gives rise to edges at ± 3.1 MHz, which are weakly visible only at a few magnetic field orientations ($B_0 = 49710$–49730 G) and cannot be easily recognized because of the complicated structure of the spectra. We note that our new hyperfine tensor values for the β_2-methylene proton, as reported in Table 1, lead to a pure dipolar tensor of -3.13 (X), 5.17 (Y), -2.03 (Z) MHz by subtracting an isotropic hyperfine coupling of 1.03 MHz. The pure dipolar tensor is in very good agreement with the theoretical values proposed by Bender *et al.* (-2.9 (X), 4.9 (Y), -1.9 (Z) MHz, (*27*)) and by Hoganson *et al.* (-2.73 (X), 4.78 (Y), -2.05 (Z) MHz, (*28*)), which supports our new assignments.

The ENDOR spectra at intermediate fields are rich in structure. For $\nu \geq |1.5|$ MHz the simulations reproduce all details with high accuracy. However, for $\nu \leq |1.5|$ MHz we are not able to simulate details around the matrix peak. Interestingly, both A_y couplings of the 2,6 and β_2-methylene protons are large (7.7 and -6.2 MHz, respectively) and do not influence the $\nu \leq |1.5|$ MHz region. The origin of the matrix peak shape is still unclear; further investigation is needed to clarify this point.

Finally, the low magnetic field region of the spectrum is accurately reproduced by our simulations. We find that the ENDOR lineshape is very sensitive to the rotation angle ϕ of the 2,6-protons in the xy-plane. An experimental spectrum and a simulation for $\phi = 25°$ are displayed in Fig. 8 (bottom). Further simulations for different angles ϕ varying from 10° to 40° are plotted in Fig. 9. Since the chemical structure of this radical is well known, it is useful to compare experiment and simulations. The noise of the spectra limits the angular resolution to only 5° and the experimental spectrum is best fit with $\phi = 25$–$30°$, which is expected for an aromatic ring proton in an sp^2 orbital.

SUMMARY

We describe the design and characteristics of a new pulsed ENDOR spectrometer operating at 140 GHz. The essential features consist of a superconducting magnet system with a ± 0.4 T sweep range and 0.2 ppm field resolution, a microwave bridge for pulsed EPR/ENDOR, and a double resonance probe. The efficiency of the probe is reflected in a absolute pulsed-EPR sensitivity of 3×10^9 spins/gauss, which should permit routine application of pulsed ENDOR, especially to samples available in limited quantities such as biologically relevant proteins. We demonstrated the capability of the spectrometer with orientation-selective ENDOR spectra of the tyrosyl radical in *E. coli* RNR. Magnetic field dependent ENDOR spectra at 140 GHz were obtained with high signal-to-noise and revealed essential new features not discerned in X-band experiments. The magnetic field dependence of the lineshape is complex, but the simulations are highly constrained and sensitive to the structural information reflected in the relative orientation of the hyperfine tensor to the electron-Zeeman g-tensor. From the analysis of experimental and simulated spectra, we obtain a new assignment for the hyperfine couplings of the weakly coupled protons of the tyrosyl radical.

ACKNOWLEDGMENTS

Thanks are accorded to Professor D.J. Singel for conversations pointing out the advantages of high frequency ENDOR. We are grateful to K. Kreischer for the loan of the frequency sweeper used in the cavity quality measurements and to Jan Henrik Ardenkjaer-Larsen (NYCOMED Innovation AB) for the gift of the trityl radical. We would like to acknowledge P. Höfer for helpful discussions and comments on this manuscript. M. Bennati thanks the Deutsche Forschungsgemeinschaft for a postdoctoral fellowship. C.T. Farrar was supported by a National Institutes of Health postdoctoral fellowship (GM-18790). This research was supported by the National Institutes of Health (grants GM-38352 and RR-00995).

REFERENCES

1. G. Feher, *Phys. Rev.* **103,** 834 (1956).
2. E. R. Davies, *Phys. Lett.* **47A,** 1–2 (1974).
3. W. B. Mims, *Proc. Roy. Soc.* **A283,** 452–457 (1965).
4. A. Grupp and M. Mehring, *in* "Modern Pulsed and CW Electron Spin Resonance" (L. Kevan and M. Bowman, Eds.), p. 195, Wiley, New York (1990).
5. C. Gemperle and A. Schweiger, *Chem. Rev.* **91,** 1481 (1991).
6. H. Thomann and M. Bernardo, *Isr. J. Chem.* **32,** 323–337 (1992).
7. W. Bryan Lynch, K. A. Earle, and J. H. Freed, *Rev. Sci. Instrum.* **59,** 1345–1351 (1988).
8. R. T. Weber, J. A. J. M. Disselhorst, L. J. Prevo, J. Schmidt, and W. T. Wenckebach, *J. Magn. Reson.* **81,** 129–144 (1989).
9. A. Y. Bresgunov, A. A. Dubinskii, V. N. Krymov, Y. G. Petrov, O. G. Poluektov, and Y. S. Lebedev, *Appl. Magn. Reson.* **2,** 715–728 (1991).
10. O. Burghaus, M. Rohrer, T. Götzinger, M. Plato, and K. Möbius, *Meas. Sci. Technol.* **3,** 765–774 (1992).
11. T. F. Prisner, S. Un, and R. G. Griffin, *Isr. J. Chem.* **32,** 357–363 (1992).
12. L. R. Becerra, G. J. Gerfen, B. F. Bellew, J. A. Bryant, D. A. Hall, S. J. Inati, R. T. Weber, S. Un, T. F. Prisner, A. E. McDermott, K. W. Fishbein, K. E. Kreischer, R. J. Temkin, D. J. Singel, and R. G. Griffin, *J. Magn. Reson. A* **117,** 8–40 (1995).
13. L. C. Brunel, A. L. Barra, and G. Martinez, *Physica B* **204,** 298–302 (1995).
14. C. Kutter, H. P. Moll, J. van Toll, H. Zuckermann, J. C. Maan, and P. Wyder, *Phys. Rev. Lett.* **74,** 2915–2928 (1995).
15. J. A. J. M. Disselhorst, H. van der Meer, O. G. Poluektov, and J. Schmidt, *J. Magn. Reson.* **116,** 183–188 (1995).
16. M. Rohrer, M. Plato, F. MacMillan, Y. Grishin, W. Lubitz, and K. Möbius, *J. Magn. Reson. A* **116,** 59–66 (1995).
17. L. Paschedag, J. van Tol, and P. Wyder, *Rev. Sci. Instrum.* **66,** 5098 (1995).
18. Y. S. Lebedev, *in* "Modern Pulsed and Continuous-Wave Electron

Spin Resonance" (L. Kevan and M. K. Bowman, Eds.), pp. 365–436, Wiley, New York (1990).

19. S. Un, J. Bryant, and R. G. Griffin, *J. Magn. Reson. A.* **101,** 92–94 (1993).

20. C. P. Poole, "Electron Spin Resonance," Wiley, New York (1983).

21. M. Rohrer, Ph.D. dissertation, Department of Physics, FU Berlin (1991).

22. D. D. Traficante and J. A. Simms, *J. Magn. Reson.* **15,** 484 (1974).

23. P. Höfer, Ph.D. dissertation, Department of Physics, University of Stuttgart (1988).

24. T. F. Prisner, M. Rohrer, and K. Möbius, *App. Magn. Reson.* **7,** 167 (1995).

25. T. F. Prisner, *Adv. Magn. Opt. Reson.* **20,** 245 (1997).

26. G. J. Gerfen, B. F. Bellew, S. Un, J. M. B. Jr., J. Stubbe, R. G. Griffin, and D. J. Singel, *J. Am. Chem. Soc.* **115,** 6420 (1993).

27. C. J. Bender, M. Sahlin, G. T. Babcock, B. A. Barry, T. K. Chandrashekar, S. P. Salowe, J. Stubbe, B. Linström, L. Petersson, A. Ehrenberg, and B.-M. Sjöberg, *J. Am. Chem. Soc.* **111,** 8076–8083 (1989).

28. C. W. Hoganson, M. Sahlin, B. M. Sjoeberg, and G. T. Babcock, *J. Am. Chem. Soc.* **118,** 4672 (1996).

29. P. J. van Dam, J. P. Willems, P. P. Schmidt, S. Poetsch, A. L. Barra, W. R. Hagen, B. M. Hoffman, K. K. Andersson, and A. Graeslund, *J. Am. Chem. Soc.* **120,** 5080–5085 (1998).